Cryo-EM reveals a new allosteric binding site at the M$_5$ mAChR

Wessel A. C. Burger[1,2,7], Jesse I. Mobbs[1,2,7], Bhavika Rana[1,2,7], Jinan Wang[3,7], Keya Joshi[3], Patrick R. Gentry[1], Mahmuda Yeasmin[1,2], Hariprasad Venugopal[4], Aaron M. Bender[5], Craig W. Lindsley[5], Yinglong Miao[3], Arthur Christopoulos[1,2,6], Celine Valant[1,2], David M. Thal[1,2].

Affiliations
1. Drug Discovery Biology, Monash Institute of Pharmaceutical Sciences, Monash University, Parkville, Victoria, Australia.
2. Australian Research Council Centre for Cryo-Electron Microscopy of Membrane Proteins, Monash Institute of Pharmaceutical Sciences, Monash University, Parkville, Victoria, Australia.
3. Computational Medicine Program and Department of Pharmacology, University of North Carolina−Chapel Hill, Chapel Hill, North Carolina 27599, United States.
4. Ramaciotti Centre for Cryo-Electron Microscopy, Monash University, Clayton, Victoria, Australia.
5. Department of Pharmacology, Warren Center for Neuroscience Drug Discovery and Department of Chemistry, Vanderbilt University, Nashville, United States
6. Neuromedicines Discovery Centre, Monash University, Parkville, Australia.
7. These authors contributed equally: Wessel A. C. Burger, Jesse I Mobbs, Bhavika Rana, Jinan Wang.

E-mail: Yinglong Miao: Yinglong_Miao@med.unc.edu; Arthur Christopoulos: arthur.christopoulos@monash.edu; Celine Valant: celine.valant@monash.edu; David M. Thal: david.thal@monash.edu

Abstract

The M$_5$ muscarinic acetylcholine receptor (M$_5$ mAChR) represents a promising therapeutic target for neurological disorders. However, the high conservation of its orthosteric binding site has posed significant challenges for drug development. While selective positive allosteric modulators (PAMs) offer a potential solution, a structural understanding of the M$_5$ mAChR and its allosteric binding sites has remained limited. Here, we present a 2.8 Å cryo-electron microscopy structure of the M$_5$ mAChR complexed with heterotrimeric G$_q$ protein and the agonist iperoxo, completing the active-state structural characterization of the mAChR family. To identify the binding site of M$_5$-selective PAMs, we implemented an integrated approach combining mutagenesis, pharmacological assays, structural biology, and molecular dynamics simulations. Our mutagenesis studies revealed that selective M$_5$ PAMs bind outside previously characterized M$_5$ mAChR allosteric sites. Subsequently, we obtained a 2.1 Å structure of M$_5$ mAChR co-bound with acetylcholine and the selective PAM VU6007678, revealing a novel allosteric pocket at the extrahelical interface between transmembrane domains 3 and 4 that was confirmed through mutagenesis and simulations. These findings demonstrate the diverse mechanisms of allosteric regulation in mAChRs and highlight the value of integrating pharmacological and structural approaches to identify novel allosteric binding sites.

Introduction

The M_5 muscarinic acetylcholine receptor (mAChR) belongs to the class A G protein-coupled receptor (GPCR) family. As one of five mAChR subtypes (M_1-M_5), it responds to the endogenous neurotransmitter acetylcholine (ACh)[1]. Despite its low expression levels in the central nervous system (CNS), the M_5 mAChR plays crucial roles, primarily localizing to dopamine-containing neurons in the substantia pars nigra and ventral tegmental areas[2–4]. Historically, drug discovery efforts targeting the M_5 mAChR concentrated on antagonists and negative allosteric modulators (NAMs). This focus stemmed from evidence that M_5 mAChR inactivation can modulate dopaminergic signalling in the CNS[5,6], suggesting therapeutic potential for substance addiction, depression, and anxiety[7–15]. However, M_5 mAChR activation may offer equally promising therapeutic applications. Studies using M_5 mAChR knockout mice revealed that this receptor mediates CNS vasculature dilation, thereby regulating cerebral blood flow[16,17]. This finding suggests that selective M_5 mAChR activation could benefit conditions such as Alzheimer's disease, schizophrenia, and ischemic stroke by enhancing CNS circulation and blood flow.

The development of selective M_5 mAChR activators faces significant challenges, primarily due to the highly conserved orthosteric acetylcholine binding site shared across all five mAChR subtypes[18,19]. This conservation has historically hindered the development of subtype-selective orthosteric ligands. To overcome this limitation, researchers shifted focus to allosteric modulators, which target spatially distinct binding sites[20]. This strategy proved promising, with several selective allosteric modulators successfully developed for the M_5 mAChR[21–26]. The selectivity of these modulators likely stems from non-conserved residues present in the allosteric binding sites, distinguishing them from the highly conserved orthosteric site.

M_5-selective positive allosteric modulators (PAMs) were initially discovered and developed based on a bromo isatin scaffold, as exemplified by the PAM VU0119498[27]. VU0119498 enhanced ACh signalling in a calcium assay at all $G\alpha_q$ coupled mAChRs (M_1, M_3, M_5) and was therefore chosen as a tool compound for further M_5 mAChR PAM optimization. A range of new M_5 mAChR PAMs were developed based on VU0119498 and these all show M_5 mAChR selectivity over all mAChR subtypes with varying levels of potency and PAM activity[21,22,24]. Unfortunately, all M_5 mAChR selective PAMs based on the isatin scaffold exhibit a poor drug metabolism and pharmacokinetic (DMPK) profile that was hard to overcome due to the intractability of the isatin scaffold in medicinal chemistry optimization[1,24].

To overcome these limitations, high-throughput screening identified a novel scaffold amenable to modification[25]. This effort led to the development of 1-((1*H*-indazol-5-yl)sulfonyl)-*N*-ethyl-*N*-(2-(trifluoromethyl)benzyl)piperidine-4-carboxamide (ML380), which emerged as the most potent M_5-selective PAM at the time[25]. ML380's ability to penetrate the CNS made it valuable for studying molecular mechanisms of allosteric modulation and as a template for further derivatives[26,28,29]. However, poor partition coefficients ultimately limited its *in vivo* utility[25]. Despite these incremental advances in developing M_5-selective PAMs, their precise allosteric binding site remained unknown, significantly limiting rational, structure-based drug design. The M_5 mAChR contains at least three known allosteric sites: the 'mAChR common' extracellular vestibule (ECV), the amiodarone-binding site[30], and the extrahelical EH4 pocket recognized by the M_5-selective NAM ML375[31]. However, none of these sites were structurally confirmed as the binding location for M_5-selective PAMs. Understanding the location of M_5-selective PAM binding site will accelerate the development of improved compounds for *in vivo* use[32]. Therefore, we initiated studies to determine the binding site of M_5-selective PAMs, beginning with ML380.

Results

ML380 does not bind to known M_5 mAChR allosteric binding sites.

To identify ML380's binding site, we first investigated its interaction with known allosteric sites through functional inositol monophosphate (IP1) accumulation assays. We tested ML380's activity on both wild-type (WT) M_5 mAChR and mutants targeting two known allosteric sites: (1) the 'common' extracellular vestibule (ECV) allosteric site[33,34], using alanine mutants, and (2) the EH4 pocket used by the M_5-selective NAM ML375[31], using mutations that convert non-conserved residues to their M_2 mAChR equivalents (A113[3.35]V, G152[4.47]A, and L156[4.51]V). These experiments measured three key parameters: ML380's affinity (pK_B), its efficacy in the system (log τ), and its functional cooperativity with ACh (log αβ)[35]. Consistent with previous studies, ML380 demonstrated both agonism and positive cooperativity with ACh at the WT M_5 mAChR[28,29] (Fig. 1a). The EH4 pocket mutant maintained ML380 function with no significant change in affinity compared to WT (Fig. 1a,c,d, Table 1). While some ECV alanine mutants showed significant differences in ML380's affinity, efficacy, and cooperativity parameters, the compound retained its ability to bind, activate, and modulate receptor function in all cases (Fig. 1b,c-e, Supplementary Fig. 1, Supplementary Table 1). These results indicated that ML380 binds neither to the common ECV allosteric site nor to the EH4 pocket used by ML375, leading us to use cryo-electron microscopy (cryo-EM) to identify its binding site.

Cryo-electron microscopy structure determination

Active state structures of the M_1-M_4 mAChRs have been determined by cryo-EM[34,36,37], leaving the M_5 mAChR as the last remaining subtype. To determine an active state M_5 mAChR structure, we engineered a modified receptor construct with several key alterations: removal of intracellular loop 3 (ICL3) residues 237-421, addition of an N-terminal HA signal sequence, and incorporation of an anti-Flag epitope tag. This modified receptor was then fused to mini-$G\alpha_{qiN}$ yielding a chimeric construct[38,39]. The receptor-G protein complex was prepared through a multi-step process including detergent solubilization for purification, stabilization with scFv16[40], addition of apyrase to hydrolyze GDP, and inclusion of 10 µM iperoxo. Prior to cryo-EM analysis, we incubated the iperoxo-bound M_5 mAChR-mini-$G\alpha_{qiN}$ complex with 10 µM ML380 overnight on ice, followed by freezing and imaging using single-particle cryo-transmission electron microscopy (TEM) on a Titan Krios microscope. The resulting structure achieved a global resolution of 2.8 Å, providing sufficient EM density maps to position the receptor and $G\alpha_{qiN}\beta_1\gamma_2$ complex (Fig. 1f, Supplementary Fig. 2-3, Supplementary Table 2). However, due to poor density, the scFv16 component was excluded from subsequent data analysis and modelling.

Analysis of the active state M_5 mAChR

The iperoxo-bound M_5 mAChR-mini-$G\alpha_{qiN}$ complex revealed iperoxo bound to the canonical mAChR orthosteric binding site, which is characterized by several key aromatic residues (Fig. 1g-h). The rotamer toggle switch residue W455[6.48] forms the binding site's floor, while three tyrosine residues (Y111[3.33], Y458[6.51], and Y481[7.39]) move inward during activation to create a tyrosine lid, separating the orthosteric site from the ECV. Consistent with previous M_1-M_4 mAChR structures[33,34,36,37], iperoxo was positioned between these aromatic residues (Fig. 1h). Additional binding site residues include the aromatic residues W162[4.57] and Y485[7.43], along with non-aromatic residues D110[3.32], N115[3.37], T194[5.39], T197[5.42], A201[5.46], N459[6.52], L188[ECL2], and C484[7.42]. Two residues play crucial roles in iperoxo recognition. Residue N459[6.52] forms hydrogen bonds with iperoxo, while D110[3.32] engages in a charge-charge interaction with iperoxo's quaternary nitrogen.

The active state M_5 mAChR displays all the hallmarks of an active state class A GPCR. Relative to the inactive state, tiotropium bound M_5 mAChR, there is an 8.1 Å outward movement of transmembrane 6 (TM6) and 4.4 Å inward movement of TM7 (Supplementary

Fig. 4). At the extracellular face, there is an outward movement of TM5 and inward movement of TM6 and extracellular loop 3 (ECL3) that lead to a contraction of the ECV (Supplementary Fig. 4b). These global changes in TM and ECL movements are mediated by changes in the conserved class A activation motifs including the $D^{3.49}R^{3.50}Y^{3.51}$, $P^{5.50}V^{3.40}F^{6.44}$, and $N^{7.49}P^{7.50}xxY^{7.53}$ motifs (Supplementary Fig. 4D, superscript refers to the Ballesteros and Weinstein scheme for conserved class A GPCR residues)[41,42].

Our active iperoxo bound M_5 mAChR structure enables the first comprehensive analysis of the entire mAChR family in their active state. Comparing this M_5 mAChR structure with other iperoxo-bound mAChR structures reveals remarkable similarity, with root mean squared deviation (RMSD) values of 0.49-0.77 Å (Fig. 2a) [33,34,36,37]. The TM domains, ECL domains, orthosteric site residues, and iperoxo positioning are nearly identical across all mAChR subtypes (Fig. 2b-d). At the receptor-G protein interface, $G\alpha_q$- and $G\alpha_{i/o}$-coupled mAChRs show distinct α5 helix insertion angles into the TM bundle (Fig. 2f-g). In $G\alpha_q$-coupled receptors (M_1, M_3, and M_5 mAChRs), the α5 helix top rotates toward TM6, while in $G\alpha_{i/o}$-coupled receptors (M_2 and M_4 mAChRs), it rotates toward TM2. This pattern, however, does not extend to the G protein N-terminus (Fig. 2e), possibly due to the varying use of scFv16, Nb35, and N-terminal chimeras across different structures. Additionally, the $G\alpha_q$-coupled M_1, M_3, and M_5 mAChR structures display a more extended and resolved TM5.

In line with our mutagenesis results (Fig. 1a-b), no cryo-EM density was observed for ML380 in the 'common' ECV allosteric site or in the EH4 binding pocket (Fig. 3a-b). Following focused refinement with a mask, some cryo-EM density was observed parallel to TM1 and TM7 in the ECV (coloured green Fig. 3c), however, this density was commonly observed in other mAChR structures and is likely a lipid molecule[43]. We also observed partial density directly below the EH4 pocket at the bottom of the TM2,3,4 interface (coloured orange in Fig. 3c). To investigate whether this partial density reflects ML380 occupancy at its allosteric binding site, we conducted radioligand binding experiments using M_5/M_2 TM chimera mutants[31]. We measured interactions between ACh and $[^3H]$-N-methyl scopolamine ($[^3H]$-NMS) with increasing ML380 concentrations. If ML380 binds at the TM2,3,4 interface, we would expect complete loss of its allosteric modulation in both M_5/M_2 TM2,3,4 and M_5/M_2 TM3,4,5 chimeras, given ML380's selectivity profile[25]. Indeed, swapping TM2-5 completely abolished ML380's ability to modulate ACh binding (Fig. 3d, Supplementary Table 3). The M_5/M_2 TM1,7,h8 chimera showed increased ML380 cooperativity, confirming that the density parallel to TM1 and TM7 is not ML380, while suggesting that exchanging these TMs affects the receptor's global activation dynamics (Fig. 3d, Supplementary Table 3).

Although the TMs 2-5 mutagenesis results were promising, the density at the TM2,3,4 interface coincides with a common cholesterol binding site in class A GPCRs[44,45], suggesting it might represent cholesterol or another lipid. For further analysis, we performed all-atom Gaussian accelerated Molecular Dynamics (GaMD) simulations on the modelled structure of the iperoxo-M_5 mAChR-mini-$G\alpha_{qiN}$ complex with ML380 bound at the TM2,3,4 interface (Fig. 3e-f). While iperoxo maintained its cryo-EM conformation with RMSD values mostly below 2 Å (Fig. 3e), ML380 showed significant fluctuations with RMSD values of ~3-8 Å compared to the initial cryo-EM pose (Fig. 3f). The combination of mutagenesis data, GaMD simulations, and ambiguous cryo-EM density did not provide convincing support for assigning ML380 to this putative allosteric binding site.

Use of an improved PAM, VU6007678, for structure determination.

To discover the allosteric binding site for selective PAMs at the M_5 mAChR, we investigated VU6007678[26], an optimized derivative of ML380's indanyl core. VU6007678 demonstrated enhanced M_5 mAChR affinity, better positive cooperativity with ACh compared to ML380[29], and significantly improved GPCR-G protein complex stabilization. To increase our chances of

obtaining a PAM-bound complex, we implemented several biochemical and pharmacological modifications. We supplemented Nb35 with scFv16 during purification for enhanced complex stability, used the endogenous agonist ACh instead of iperoxo, and maintained VU6007678 at 10 µM throughout purification rather than adding it before grid freezing as with ML380. These modifications improved protein purification efficiency, yielding a sample at 18 mg/mL. When applied to Au grids, the sample produced a complex resolved to 2.1 Å from 418,794 particles (Fig. 4a, Supplementary Fig. 2-3).

The high-quality cryo-EM density maps enabled precise placement of the receptor, $G\alpha_{qiN}$ $\beta_1\gamma_2$, Nb35, and scFv16, with clear sidechain orientations for most amino acids. The ACh-VU6007678 structure closely resembles the iperoxo structure, showing an RMSD value of 0.49 Å (Supplementary Fig. 5a-d). The orthosteric binding pocket shows well-resolved density for ACh positioned beneath the tyrosine lid residues and above $W455^{6.48}$ (Fig 4b-c). While ACh engages the same orthosteric binding pocket residues as iperoxo with similar orientations, $W455^{6.48}$ adopts a more horizontal and planar orientation with ACh-bound, similar to observations in the M_4 mAChR with ACh and iperoxo[34] (Fig. 4e). ACh forms key interactions within the orthosteric binding pocket through its quaternary ammonium group and acetyl moiety (Fig. 4f,g). The positively charged quaternary ammonium establishes a cation-π interaction with the aromatic cage formed by $Y111^{3.33}$, $W455^{6.48}$, $Y458^{6.51}$, and $Y481^{7.39}$, while also engaging in a charge-charge interaction with $D110^{3.32}$. The acetyl group of ACh forms a hydrogen bond with a water molecule that coordinates with $N459^{6.52}$ (Fig. 4g) altogether anchoring ACh in an orientation that promotes receptor activation.

Clear, well-defined density unambiguously corresponding to VU6007678 was detected at the intracellular interface of TM3,4 and above ICL2 (Fig. 4a, b, d). The extended binding site accommodates VU6007678 through multiple interactions with the M_5 mAChR (Fig. 4i, k). The indanyl core, positioned at the top of the allosteric binding site, forms hydrophobic interactions with $M150^{4.45}$, $F126^{3.48}$, and $V123^{3.45}$, while engaging in an edge-to-face π-interaction with $F130^{3.52}$. The propyl chain extends toward TM4, forming a hydrophobic interaction with $I149^{4.44}$. Hydrogen bonding occurs between the carboxamide with $R146^{4.41}$ and between the sulfonyl and $K141^{ICL2}$. The indazole of VU6007678 forms a π-π interaction with $F130^{3.52}$, a cation-π interaction with $R134^{3.56}$ and at the bottom of TM3, and a hydrophobic interaction with $Y129^{3.51}$. Other residues that make up the VU6007675 binding site include $Y68^{2.42}$ and $Y138^{ICL2}$. These extensive interactions likely explain why VU6007678 has high cooperativity with ACh and its high affinity for the M_5 mAChR active state. Given the low affinity of VU6007678 for the inactive state M_5 mAChR, as observed in radioligand binding with antagonist [³H]-NMS[29], we hypothesized that these binding site residues undergo substantial rearrangement during activation. Superimposition of the ACh-VU6007678 structure with the inactive tiotropium-bound M_5 mAChR crystal structure[18] revealed significant conformational changes in the allosteric binding site. $F130^{3.52}$, $Y138^{ICL2}$, and $K141^{ICL2}$ show marked inward movement toward the TM core, while $R134^{3.56}$ moves outward (Fig. 4j). These coordinated conformational changes create the allosteric binding site (Supplementary Fig. 5e,f) enabling VU6007678 binding and explaining its state-dependent affinity profile.

We performed GaMD simulations on the ACh-VU6007678-bound M_5 mAChR-mini-$G\alpha_{qiN}$ complex to validate the binding pose of VU6007678 and examine its dynamic interactions with the receptor. Both ACh and VU6007678 maintained stable positions throughout the simulation, with ACh showing minimal fluctuations (RMSD = 1.70 ± 0.28 Å) and VU6007678 displaying moderate mobility while remaining in its binding pocket (RMSD = 4.85 ± 0.56 Å) (Fig. 4h, l).

The VU6007678 binding site contains several residues that vary across mAChR subtypes (Fig. 5a). While $Y68^{2.42}$ is unique to M_5, appearing as phenylalanine in other mAChRs, $R134^{3.56}$ and $R146^{4.41}$ are conserved among M_1, M3, and M_5 but differ in M_2 and M4. $V123^{3.45}$ varies between leucine, isoleucine, and valine across M_1-M_4, while $I149^{4.44}$ alternates between

leucine, methionine, and valine in these subtypes. The ICL2 lysine is conserved in M_1-M_3 but appears as arginine in M_4. In contrast, F126$^{3.48}$, F130$^{3.52}$, T133$^{3.55}$, Y138^{ICL2}, and M150$^{4.45}$ remain fully conserved across all five mAChR subtypes. This partially non-conserved binding site architecture provided an opportunity to further validate and characterize the binding site through mutagenesis studies and functional assessment using the TruPath G protein activation assay[46].

In WT M_5 mAChR, VU6007678 demonstrated robust positive functional cooperativity with ACh signalling and exhibited significant allosteric agonism (Fig. 5b) in a G_q TruPath experiment. Given the selectivity of VU6007678 for the M_5 mAChR over the M_2 mAChR and its extensive ICL2 interactions, we first investigated non-conserved residues at the bottom of TMs 3, 4, and ICL2 by mutating them to their M_2 mAChR counterparts. A construct containing multiple mutations (S131$^{3.53}$C, I132$^{3.54}$V, R134$^{3.56}$K, R139^{ICL2}P, A140^{ICL2}V, P144$^{4.39}$T, R146$^{4.41}$M, I149$^{4.44}$M, G152$^{4.47}$A, and L153$^{4.48}$A (referred to as the M_5/M_2 swap) caused a complete loss in the ability of VU6007678 to modulate ACh signalling and to display allosteric agonism (Fig. 5c). Individual residue analysis revealed that the R146$^{4.41}$M mutation reduced functional modulation and eliminated allosteric agonism, while the F130$^{3.52}$M mutation completely abolished the affinity, functional modulation, and agonism of VU6007678 (Fig. 5d-f, Supplementary Fig. 6). These effects align with our structural data with R146$^{4.41}$ forming a hydrogen bond with the carboxamide group of VU6007678, and a π-interaction between F130$^{3.52}$ and the indanyl core of VU6007678 (Fig. 4i). Other single mutations (Y68$^{2.42}$F, V123$^{3.45}$I, T133$^{3.55}$A, R134$^{3.56}$A, R134$^{3.56}$K, K141^{ICL2}A, R146$^{4.41}$M) showed no significant changes in affinity, functional modulation, or allosteric agonism (Fig. 5d-f, Supplementary Fig. 6).

Radioligand binding studies of F130$^{3.52}$M, R146$^{4.41}$M, and the M_5/M_2 swap showed no significant change in VU6007678 affinity (Fig. 5g, Supplementary Fig. 7, Table 4). While the binding cooperativity (log α) was reduced in these constructs (Fig. 5h, Supplementary Fig. 7, Table 4), the values were not significantly different from WT M_5 mAChR, likely due to higher uncertainty in the parameter calculations for the F130$^{3.52}$M and M_5/M_2 swap constructs. The degree of efficacy modulation (β) by VU6007678 on ACh can be calculated by subtracting the binding modulation (log α) from the functional modulation (log αβ)[34]. This calculation at WT M_5 mAChR yielded a log β value of 0.4 ± 0.2, indicating that VU6007678's allosteric effect is primarily mediated through binding cooperativity, with a smaller contribution from efficacy modulation. This value could only be compared to the R146$^{4.41}$M mutant, as the F130$^{3.52}$M and M_5/M_2 swap showed no functional modulation. The R146$^{4.41}$M mutant yielded a log β value of -0.7 ± 0.3, suggesting impaired efficacy modulation by VU6007678. These findings are supported by our previous characterisation of VU6007678 in receptor alkylation studies, which revealed modest efficacy modulation in functional IP one assays[29]. Interestingly, this observation was unique to VU6007678 in the structure-activity relationship (SAR) study. Collectively, these data highlight the importance of the VU6007678 binding site residues in mediating both functional and efficacy modulation, possibly due to the binding site's location overlapping the DRY activation motif and its proximity to the G protein binding site.

Further validation of the allosteric binding site through GaMD simulations revealed key interactions between VU6007678 and receptor residues. The PAM formed stable interactions with F130$^{3.52}$, R146$^{4.41}$, and M150$^{4.45}$ (Fig. 5i-k), consistent with both the cryo-EM structure and mutagenesis data. In contrast, hydrogen bond interactions between VU6007678 and receptor residues R134$^{3.56}$, T133$^{3.55}$, and K141^{ICL2} showed greater variability with larger distances and higher fluctuations (Supplementary Fig. 8), aligning with our experimental observations where mutations of these residues did not significantly affect VU6007678 function. These results highlight how VU6007678 engages with residues involved in the inactive-to-active transition of the M_5 mAChR, particularly through stable interactions with F130$^{3.52}$ and R146$^{4.41}$, while maintaining more dynamic interactions with K141^{ICL2}. Together, this suggests VU6007678 helps stabilize key residues involved in receptor activation.

Discussion

Allosteric modulators for the mAChRs have long been pursued for selective targeting of a specific mAChR subtype. Whilst selective allosteric modulators for the M_5 mAChR have been discovered, the development and application of these have lagged compared to allosteric modulators selective for other mAChRs, particularly the M_1 and M_4 mAChR. This partly reflects the limited structural knowledge of the M_5 mAChR overall, as well as the specific lack of insight into the allosteric binding site for M_5-selective PAMs. Here we present a cryo-EM structure of the M_5 mAChR bound to the orthosteric agonist iperoxo that 'completes' the active state structure ensemble for all five mAChR subtypes. Initial attempts to solve an allosteric modulator co-bound structure with ML380 and iperoxo were unsuccessful. Yet through use of analytical pharmacology to determine the optimum orthosteric and allosteric ligand combination and improved biochemical techniques, we obtained a high-resolution structure of the M_5 mAChR co-bound to the endogenous orthosteric agonist ACh and the selective PAM VU6007678. Our data begins to explain several facets of selective allosteric modulation at the M_5 mAChR including 1) the historic difficulties in developing subtype selective PAMs for this mAChR subtype, 2) how changes to ML380 led to the improved PAM VU6007678, 3) subtype selectivity, and 4) mechanism of action.

The *in vivo* translation of M_5 mAChR selective PAMs has been plagued by issues relating to DMPK and suboptimal partition coefficients (K_p)[25]. The observation that the allosteric binding site for VU6007678 is in the TM bundle partially explains this, as to reach this allosteric binding site, modulators must display a high degree of lipophilicity. Despite this, the VU6007678 scaffold offers numerous opportunities for modifications, and our structure will aid the process of developing improved allosteric modulators as it provides information on the molecular interactions that occur between VU6007678 and the M_5 mAChR at its allosteric binding site. Specifically, Y68$^{2.42}$ is the only residue within the allosteric binding site that is different at all M_1-M_4 mAChR subtypes. It may therefore be possible to introduce and optimize the presence of various polar functional groups on the indanyl core to promote hydrogen bonding between the ligand and receptor and enhance affinity whilst reducing the compound's lipophilicity. Note, the compounds reported in the previous SAR series all had a fluorine functional group attached to the indanyl core[26]. Enhancing the selectivity of PAMs for the M_5 mAChR will be, in part, crucial to the future clinical success of M_5 mAChR PAMs. All M_5 PAMs discovered to date display activity at the M_1 and M_3 mAChRs whilst they are most selective against the M_2 and M_4 mAChR where they display very little to no activity. Analysis of the residues within the VU6007678 allosteric binding site may explain the basis for this as R134$^{3.56}$ and R146$^{4.41}$ are fully conserved between the M_5 mAChR and M_1/M_3 mAChRs and non-conserved between the M_5 mAChR and the M_2/M_4 mAChRs.

Despite the absence of an ML380-bound M_5 mAChR structure, given that VU6007678 is a derivative of ML380, predictions on how ML380 interacts with this site can be made. This allows for an explanation of how the changes to VU6007678 led to an improved PAM. The extension of the ethyl present in ML380 into a propyl group at VU6007678 gives rise to an extra interaction with I149$^{4.44}$. In addition, the substitution of the trifluoromethylbenzyl group at ML380 with the indanyl group gives rise to more hydrophobic interactions and greater engagement with the top of the allosteric site consisting of V123$^{3.45}$, F126$^{3.48}$ and M150$^{4.45}$ where edge-to-face π-interaction takes place with F126$^{3.48}$.

Our structure offers a few observations on the mechanism of action for PAMs at the M_5 mAChR. First, the allosteric binding site of VU6007678 is in close proximity to the highly conserved DRY activation motif, indicating that PAM binding at this allosteric site stabilizes the active state of the M_5 mAChR. Second, the mAChR family has served as a model receptor family for the study of allosteric modulation at GPCRs[19]. Despite a wealth of mAChR allosteric modulators with different scaffolds available, this is only the second site to be confirmed by

structural biology studies at the mAChRs[33,34] (Fig. 6a). All PAMs discovered to date bind to the mAChRs at what is termed the common ECV allosteric site in a solvent accessible vestibule on top of the orthosteric binding site. Here PAMs exert their mechanism of action through two mechanisms, trapping the orthosteric ligand in the orthosteric site through stabilising the active state and sterically hindering the orthosteric ligand dissociation[47,48]. Due to the distal location of this allosteric binding site to the mAChR orthosteric site, this would indicate PAMs exert their mechanism of action through this site only by stabilising the active state. Such a mechanism would be akin to that observed for other allosteric modulators binding to the same site at different GPCRs[49], including but not limited to, compound 6FA at the β_2AR[50] and LY3154207 at the D1R[51–53]. The discovery of a methionine ($M^{4.45}$) within the VU6007678 allosteric binding site allows for potential methionine labelling of this residue. Subsequent characterisation of PAM activity at a methionine labelled M_5 mAChR through spectroscopic approaches will facilitate further exploration of how PAMs exert their mechanism of action at the M_5 mAChR as was done for LY2119620 at the M_2 mAChR[54].

At the bottom of the TM2,3,4 interface of the ACh-VU6007678 structure we observed well defined densities that likely correspond to three cholesterol molecules (Fig. 6b). Note in our iperoxo structure this site was occupied by partial density that we cautiously hypothesised could be ML380. Considering the much higher resolution of the ACh-VU6007678 structure, and assignment of the VU6007678 binding site at the bottom of the extrahelical interface at TMs3-4, it is likely that the density present in the iperoxo-bound structure represents cholesterol molecules. Especially given that this site is recognised as a common cholesterol site within class A GPCRs[44,55] and that neurosteroids and steroid hormones, including derivatives of cholesterol, have displayed modulatory properties at the M_5 mAChR[56,57]. Due to the lower density and map quality in this region, conclusive assignment of this density to either ML380 or cholesterol was difficult in the iperoxo structure, highlighting the map quality that is required to conclusively assign density to small molecules. Particularly at extrahelical regions where a number of lipid and cholesterol molecules may be present.

Altogether and more broadly, the discovery of this novel allosteric binding site at the M_5 mAChR adds to the knowledge of allostery at the mAChR, specifically on how allosteric modulators engage with the mAChRs, and provides an additional avenue through which to target these highly conserved proteins.

Materials and Methods

Receptor & G protein co-expression

A modified M_5 mAChR construct was used where residues 237-421 of ICL3 were removed and HA signal sequence and anti-Flag epitope tag were added to the N terminus. Modified M_5 mAChR was fused to a mini-Gα_{qiN} chimeric construct that is a mini-Gα_s substituted with Gα_q residues at the receptor interface and the αN of Gα_i[38,39]. A 3C protease recognition site and GGGS linker was used to separate the receptor and G protein. The fused $M_{5\Delta ICL3}$mGα_{sQi}/construct was cloned into a pFastbac baculovirus transfer vector. G protein β_1 and γ_2 subunits were cloned into a pVL1392 baculovirus transfer vector with the β subunit modified to contain a carboxy (C)-terminal 8× histidine tag. *Trichoplusia ni* (Hi5) insect cells were grown in ESF 921 serum-free media (Expression Systems) and infected at a density of 4.0×10^6 cells per millilitre with a 1:1 ratio of $M_{5\Delta ICL3}$mGα_{sQi} to G$\beta_1\gamma_2$ viruses and shaken at 27°C for 48-60 hours. Cells were harvested by centrifugation and cell pellets were flash frozen using liquid nitrogen and stored at -80°C.

Single chain stabilising fragment expression and purification

A single-chain construct of Fab16 (scFv16), tagged with an 8× histidine sequence at the C-terminus, was cloned into a modified pVL1392 baculovirus transfer vector for secreted expression in *Trichoplusia ni* (Hi5) insect cells (Expression Systems). The cells were cultured in serum-free ESF 921 media (Expression Systems), infected at a density of 4.0×10^6 cells per millilitre, and incubated with shaking at 27°C for 48-72 hours. For purification, the pH of the supernatant from the baculovirus-infected cells was adjusted with Tris pH 8.0. Chelators were neutralized by adding 5 mM $CaCl_2$ and stirring the solution for 1 hour at 25°C. Precipitates were cleared by centrifugation, and the supernatant was then applied to Ni-NTA resin. The column was washed with a solution of 20 mM Hepes pH 7.5, 50 mM NaCl, and 10 mM imidazole, followed by a second wash containing the same buffer with 100 mM NaCl. The scFv16 protein was eluted using the low-salt buffer with 250 mM imidazole. SDS-PAGE with Coomassie staining was used to assess purity of the eluted protein. Finally, the sample was concentrated, flash-frozen in liquid nitrogen, and stored at -80°C.

Nb35 expression and purification

Nb35 was expressed in the periplasm of the BL21(DE3) Rosetta *Escherichia coli* cell line using an autoinduction approach[58]. Transformed cells were cultured at 37°C in a modified ZY medium containing 50 mM phosphate buffer (pH 7.2), 2% tryptone, 0.5% yeast extract, 0.5% NaCl, 0.6% glycerol, 0.05% glucose, and 0.2% lactose, with 100 µg/ml carbenicillin and 35 µg/ml chloramphenicol. When the culture reached an OD600 of 0.7, the temperature was reduced to 20°C for approximately 16 hours, after which cells were harvested by centrifugation and stored at −80°C. To purify, cells were lysed in ice-cold buffer (0.2 M Tris pH 8.0, 0.5 M sucrose, 0.5 M EDTA) at a ratio of 1g of cell pellet to 5mL of lysis buffer for 1 hour at 4°C. 2x volume of ice cold MQ was added and incubated for an additional 45 minutes at 4°C. Lysate was centrifuged to remove cell debris and supernatant containing Nb35 was spiked with 20 mM HEPES pH 7.5, 150 mM NaCl, 5 mM $MgCl_2$, 5 mM Imidazole and applied to Ni-NTA resin followed by 90 minutes incubation at 4°C. The column was washed with 40 column volumes (CV) of wash buffer (20 mM HEPES pH 7.5, 500 mM NaCl, 5 mM Imidazole) and eluted with elution buffer (20 mM HEPES pH 7.5, 100 mM NaCl, 250 mM Imidazole). Elute was concentrated and stored at 80°C.

Complex purification

Iperoxo-bound M_5 mAChR-mini-Gα_{qiN} complex

$M_{5\Delta ICL3}$ mGα_{sQi} co-expressed with G$\beta_1\gamma_2$ was thawed and lysed in in 20 mM HEPES pH 7.4, 5 mM $MgCl_2$, 1 µM Ipx and protease inhibitors (500 µM PMSF, 1 mM LT, 1 mM benzamidine). The sample was rotated at room temperature for 15 minutes and spiked with apyrase towards the end of the 15 minutes. The pellet was spun down by centrifugation and solubilized in 20

mM HEPES pH 7.4, 100 mM NaCl, 5 mM $MgCl_2$, 5 mM $CaCl_2$, 0.5% LMNG (Anatrace, Maumee, OH, USA), 10 µM Ipx, and protease inhibitors (500 µM PMSF, 1 mM LT, 1 mM benzamidine). The resuspended pellet was homogenised in a Dounce homogeniser and complex formation was initiated through addition of scFv16. The sample was incubated with stirring at 4°C for 2 hours followed by centrifugation to remove insoluble material. Solubilised complex was bound to equilibrated M1 anti-Flag affinity resin though batch binding at room temperature for 1 hour. The resin was packed into a glass column and washed with 20 mM HEPES pH 7.4, 100 mM NaCl, 5 mM $MgCl_2$, 5 mM $CaCl_2$, 0.01% LMNG, and 1 µM Ipx until no more protein was coming off the column as determined by Bradford. Complex was eluted using 20 mM HEPES pH 7.4, 100 mM NaCl, 5 mM $MgCl_2$, 0.01% LMNG, and 1 µM Ipx in the presence of 5 mM EDTA and 0.1 mg/ml Flag peptide. Eluted complex was concentrated in an Amicon Ultra-15 100 kDa molecular mass cut-off centrifugal filter unit (Millipore, Burlington, MA, USA) and purified by size exclusion chromatography (SEC) on a Superdex 200 Increase 10/300 GL (Cytiva, Marlborough, MA, USA) in 20 mM HEPES pH 7.4, 100 mM NaCl, 5 mM $MgCl_2$, 0.01% LMNG, and 1 µM Ipx. Fractions containing complex (as determined by SDS-page and Coomassie staining) were pooled and concentrated to 3.5 mg/mL, flash frozen using liquid nitrogen and stored at −80°C.

ACh-VU6007678-bound M_5 mAChR-mini-$G\alpha_{qiN}$ complex
The ACh-VU6007678 M_5 mAChR sample was purified in an identical manner with the following changes; 1) complex formation was initiated through addition of scFv16 and Nb35, 2) ACh was included in all buffers at 100 µM until SEC where a concentration of 10 µM was utilised, 3) VU6007678 was present throughout the purification at a concentration of 10 µM. The final purified product was concentrated to 18 mg/mL.

Vitrified sample preparation and data collection
For the iperoxo-M_5 mAChR sample, EMAsian - TiNi 200 mesh 1.2/1.3TiNi 200 mesh 1.2/1.3 grids were glow discharged using Pelco EasyGlow for 90 seconds with 15-mA current. Prior to grid freezing, the iperoxo-M_5 mAChR sample was spiked with 30 µM of ML380 and incubated ON at 4°C. A 3 µL of this spiked sample was applied and flash frozen in liquid ethane using a Vitrobot markIV with a blot force of 4 and blot time of 2 seconds at 100 % humidity and 4 °C. Data were collected on a Titan Krios (Thermo Fisher Scientific) 300 kV electron microscope equipped with a K3 detector, 50 µm C2 aperture, no objective aperture inserted, indicated magnification x 130 000 in nanoprobe TEM mode, a slit width of 10eV, pixel size 0.65 Å, exposure rate 10.57 counts per pixel per second, exposure time 2.68 s, total exposure 60 e $Å^{-2}$, and 60 frames. In total, 9104 movies were collected.

For the ACh-VU6007678 M_5 mAChR sample, 3 µL of sample was applied to glow-discharged (15 mA, 180 s) UltrAufoil R1.2/1.3 300 mesh holey grid (Quantifoil) and were frozen in liquid ethane using a Vitrobot mark IV (Thermo Fisher Scientific) at 100% humidity and 4°C with a blot time of 2 s and blot force of 10. The sample was collected similarly, except at 105kX magnification with a pixel size of 0.82 Å, and 7489 movies were collected.

Image Processing
For the iperoxo-M_5 mAChR sample, 9104 movies were collected and adjusted for beam-induced motion by MotionCor2[59]. Non-dose weighted micrographs were used for CTF estimation using Gctf[60]. 8341 micrographs were identified as having a ctf fit resolution below 4 Å, and these were selected for further examination. 3,833,583 particles were autopicked using Gautomatch (https://www2.mrc-lmb.cam.ac.uk/research/locally-developed-software/zhang-software/#gauto). The particles were extracted with relion-3.1[61] and then imported into CryoSparc[62] for rounds of 2D classification, ab initio 3D and 3D refinement to obtain a 3.04 Å model. Particles were taken to Relion3.1 for polishing and subsequent 3D refinement back in Cryosparc yielded a final model of 2.75 Å based on the gold standard Fourier shell correlation cut-off of 0.143 from 426,714 particles. A further local refinement was performed to generate a receptor-focused map (2.67 Å).

The ACh-VU6007678 M_5 mAChR sample was processed similarly. 7489 movies were collected and adjusted for beam-induced motion by MotionCor2[59]. Non-dose weighted micrographs were used for CTF estimation using Gctf[60]. 4,436,835 particles were autopicked using Gautomatch (https://www2.mrc-lmb.cam.ac.uk/research/locally-developed-software/zhang-software/#gauto). The particles were extracted with relion-3.1[61] and then imported into CryoSparc[62] for rounds of 2D-classification and heterogenous refinement. A set of particles (~900k) were polished in relion3.1 and a final round of 3D-classification (no alignment) was performed. This final set of 418,794 particles were finally subjected to non-uniform refinement with CTF-refinement in CryoSparc, resulting in a final map of 2.06 Å based on the gold standard Fourier shell correlation cut-off of 0.143. A further local refinement was performed to generate a receptor-focused map (2.11 Å).

Model building and refinement

An initial receptor model was generated from the cryo-EM structure of the M_4 mAChR receptor (PDB: 7TRP). An initial model for the G protein (mini-$G\alpha_{qiN}$:$G\beta_1G\gamma_2$:ScFv16) was generated from the CCK1:mini-$G\alpha_{qiN}$ complex (PDB: 7MBY). Initial models were placed in the EM maps using UCSF ChimeraX[63] and rigid-body-fit using PHENIX[64]. Models were refined with iterative rounds of manual model building in Coot[65] and ISOLDE, and real-space refinement in PHENIX. Ligands ACh and iperoxo were obtained from the monomer library, while initial model and restraints for VU6007678 were generated using the GRADE web server (https://grade.globalphasing.org). Model validation was performed with MolProbity[66] and the wwPDB validation server[67]. Figures were generated with UCSF ChimeraX and PyMOL (Schrödinger).

Cell culture

FlpIn Chinese hamster ovary (CHO) cells (Thermo Fisher Scientific) stably expressing M_5 mAChR constructs were cultured at 37°C in 5% CO_2 using Dulbecco's modified Eagle's medium (DMEM; Invitrogen) supplemented with 5% foetal bovine serum (FBS; ThermoTrace). At confluence, media was removed, and cells were washed with phosphate-buffered saline (PBS) and harvested from tissue culture flasks using versene (PBS with 0.02% EDTA). The cells were pelleted by centrifugation at 350g for three minutes and then resuspended in DMEM with 5% FBS. Subsequently, the cells were either plated for an assay or reseeded into a tissue culture flask.

Inositol Monophosphate (IP1) Accumulation Assay

FlpIn CHO cells stably expressing either WT or mutant hM_5 mAChR were seeded in clear, flat-bottom 96-well plates at a density of 10,000−25,000 cells per well (depending on the cell line) one day prior to the assay. The optimal cell density for each line was chosen based on achieving an IP1 response that fell within the linear range of the IP1 standard curve. On the assay day, the medium was replaced with stimulation buffer (Hanks' balanced salt solution (HBSS) containing 10 mM HEPES, 1.3 mM $CaCl_2$, and 30 mM LiCl, pH 7.4) and allowed to incubate for 60 minutes at 37°C before ligand stimulation. After this pre-incubation, the buffer was replaced, and cells were exposed to ligands for 60 minutes at 37°C in a 5% CO_2 atmosphere, with a total assay volume of 100 µL. Following the 60-minute stimulation, ligands were removed by rapid removal of buffer. Cells were lysed by freeze-thawing in 30 µL of stimulation buffer. IP1 accumulation was then quantified using the HTRF IP-One assay kit (Cisbio), with fluorescence measured on an EnVision multilabel plate reader (PerkinElmer).

TruPath – G protein Activation Assay

Upon reaching 60-80% confluence, FlpIn CHO cells stably expressing WT or mutant hM_5 mAChR were transiently transfected using Polyethylenimine (PEI; Sigma-Aldrich). For each well, 10 ng of each plasmid (pcDNA5/FRT/TO-$G\alpha_{i1}$-RLuc8, pcDNA3.1-β_3, and pcDNA3.1-$G\gamma_9$-GFP2) was added in a 1:1:1 ratio, totalling 30 ng. These plasmids were generously provided by Prof. Bryan Roth from the University of North Carolina. The cells were then plated at 30,000

cells per well into 96-well Greiner CELLSTAR white-walled plates (Sigma-Aldrich). After 48 hours, the cells were washed with 200 µL PBS and replaced with 1x HBSS supplemented with 10 mM HEPES. The cells were incubated for 30 minutes at 37°C before adding 10 µL of 1.3 µM Prolume Purple coelenterazine (Nanolight Technology, Pinetop, AZ). Following a further 10-minute incubation at 37°C, bioluminescence resonance energy transfer (BRET) measurements were performed using a PHERAstar FSX plate reader (BMG Labtech) with 410/80-nm and 515/30-nm filters. Four baseline measurements were taken before adding drugs or vehicle, bringing the final assay volume to 100 µL, followed 10 more minutes of readings. The BRET signal was calculated as the ratio of 515/30-nm emission to 410/80-nm emission. This ratio was vehicle-corrected using the initial four baseline measurements and then baseline-corrected again using the vehicle-treated wells. Data were normalized to the maximum ACh response to allow for grouping of results.

Radioligand Binding

FlpIn CHO cells stably expressing WT hM_5 mAChR or mutants were plated at 25,000 cells per well in 96-well isoplates (PerkinElmer Life Sciences) and incubated overnight at 37°C in a 5% CO_2 incubator. The following day, the cells were washed with PBS and incubated in 20 mM HEPES, 100 mM NaCl, 10 mM $MgCl_2$, pH 7.4. For saturation binding experiments, the cells were incubated with varying concentrations of the orthosteric antagonist [^{3}H]-*N*-methylscopolamine ([^{3}H]-NMS; specific activity, 70 Ci/mmol, Perkin Elmer) in a final volume of 100 µL for 6 hours at room temperature. For interaction experiments between orthosteric agonist and allosteric modulator, competition binding was performed between a K_D concentration of [^{3}H]-NMS and varying concentrations of an orthosteric drug in the presence of different concentrations of an allosteric modulator, in a total volume of 100 µL binding buffer. For all experiments, non-specific binding was defined using 10 µM of atropine. The assay was terminated by the rapid removal of the radioligand, followed by two 100 µL washes with ice-cold 0.9% NaCl buffer. Radioactivity was measured by adding 100 µL of Optiphase Supermix scintillation fluid (Perkin Elmer) and counted using a MicroBeta^2 Plate Counter (PerkinElmer Life Sciences).

Data Analysis

All data were analyzed using GraphPad Prism 10 (GraphPad Software, San Diego, CA). The interaction between orthosteric agonist and allosteric modulator in functional assays was analysed using an operational model of allosterism to determine functional modulation (log αβ) and affinity (pK_B) parameters[35]. Radioligand saturation binding experiments with [^{3}H]-NMS to determine B_{max} and pK_D values were determined as previously described[31]. For the radioligand binding interaction of orthosteric agonist with various concentrations of allosteric modulator, the data were fit to an allosteric ternary complex model to derive pK_B and α binding cooperativity parameters[68]. All affinity, potency, cooperativity, and efficacy parameters were estimated as logarithms. Statistical analysis between different treatment conditions was performed using one-way ANOVA, with a p-value of < 0.05 considered significant.

Gaussian accelerated Molecular Dynamics (GaMD)

GaMD is an enhanced sampling method that works by adding a harmonic boost potential to reduce the system energy barriers[69,70]. When the system potential $V(\vec{r})$ is lower than a reference energy E, the modified potential $V^*(\vec{r})$ of the system is calculated as:

$$V^*(\vec{r})=V(\vec{r})+\Delta V(\vec{r})$$

$$\Delta V(\vec{r})=\begin{cases} \frac{1}{2}k\left(E-V(\vec{r})\right)^2, & V(\vec{r})<E \\ 0, & V(\vec{r})\geq E, \end{cases} \tag{1}$$

where *k* is the harmonic force constant. The two adjustable parameters E and k are automatically determined on three enhanced sampling principles. First, for any two arbitrary

potential values $v_1(\vec{r})$ and $v_2(\vec{r})$ found on the original energy surface, if $V_1(\vec{r}) < V_2(\vec{r})$, ΔV should be a monotonic function that does not change the relative order of the biased potential values; i.e., $V_1^*(\vec{r}) < V_2^*(\vec{r})$. Second, if $V_1(\vec{r}) < V_2(\vec{r})$, the potential difference observed on the smoothened energy surface should be smaller than that of the original; i.e., $V_2^*(\vec{r}) - V_1^*(\vec{r}) < V_2(\vec{r}) - V_1(\vec{r})$. By combining the first two criteria and plugging in the formula of $V^*(\vec{r})$ and ΔV, we obtain:

$$V_{max} \leq E \leq V_{min} + \frac{1}{k}, \tag{2}$$

Where V_{min} and V_{max} are the system minimum and maximum potential energies. To ensure that Eq. 2 is valid, k has to satisfy: $k \leq 1/(V_{max} - V_{min})$. Let us define: $k = k_0 \cdot 1/(V_{max} - V_{min})$, then $0 < k_0 \leq 1$. Third, the standard deviation (SD) of ΔV needs to be small enough (i.e. narrow distribution) to ensure accurate reweighting using cumulant expansion to the second order: $\sigma_{\Delta V} = k(E - V_{avg})\sigma_V \leq \sigma_0$, where V_{avg} and σ_V are the average and SD of ΔV with σ_0 as a user-specified upper limit (e.g., $10k_B T$) for accurate reweighting. When E is set to the lower bound $E = V_{max}$ according to Eq. 2, k_0 can be calculated as:

$$k_0 = \min(1.0, k_0') = \min\left(1.0, \frac{\sigma_0}{\sigma_V} \cdot \frac{V_{max} - V_{min}}{V_{max} - V_{avg}}\right), \tag{3}$$

Alternatively, when the threshold energy E is set to its upper bound $E = V_{min} + 1/k$, k_0 is set to:

$$k_0 = k_0'' \equiv \left(1 - \frac{\sigma_0}{\sigma_V}\right) \cdot \frac{V_{max} - V_{min}}{V_{avg} - V_{min}}, \tag{4}$$

If k_0'' is calculated between 0 and 1. Otherwise, k_0 is calculated using Eq. 3.

GaMD Simulations and Simulation Analysis

The cryo-EM structures of the ACh-VU6007678-bound M_5 mAChR-mini-Gα_{qiN} complex and the Iperoxo-bound M_5 mAChR-mini-Gα_{qiN} complex were used to set up simulation systems. The initial model of the Iperoxo-ML380-bound M_5 mAChR-mini-Gα_{qiN} complex was created by docking ML380 into the bottom of the TM2,3,4 interface. As in our previous studies[34], the intracellular loop 3 (ICL3) of the receptor and the α-helical domain of the G protein, which were missing in the cryo-EM structure, were not modeled. The MD simulation systems were prepared by inserting the ACh-VU6007678-bound M_5 mAChR-mini-Gα_{qiN} and the Iperoxo-bound M_5 mAChR-mini-Gα_{qiN} complexes into a POPC (palmitoyl-2-oleoyl-sn-glycero-3-phosphocholine) lipid bilayer using VMD (Visual Molecular Dynamics). In each simulation system, the protein and lipid bilayer were solvated with TIP3P water molecules in a box of 12.5 nm x 12.5 nm x 14.0 nm with the periodic boundary condition. The system charge was neutralized with 150 mM NaCl. The AMBER FF14SB force field[71] was applied for the proteins, while the AMBER LIPID21 force field[72] was used for the lipids. The general amber force field (GAFF2) parameters[73] for ACh, Iperoxo, ML380, and VU6007678 were generated with ANTECHAMBER. The two simulation systems were first energy minimized for 5,000 steps with constraints on the heavy atoms of the proteins and phosphor atom of the lipids. The hydrogen-heavy atom bonds were constrained using the SHAKE algorithm and the simulation time step was set to 2.0 fs. The particle mesh Ewald (PME) method[74] was employed to compute the long-range electrostatic interactions and a cutoff value of 9.0 Å was applied to treat the non-bonded atomic interactions. The temperature was controlled using the Langevin thermostat with a collision frequency of 1.0 ps^{-1}. Each system was equilibrated using the constant number, volume, and temperature (NVT) ensemble at 310K for 250 ps and under the constant number, pressure, and temperature (NPT) ensemble at 310 K and 1 bar for another 1 ns with constraints on the heavy atoms of the protein, followed by 10 ns short conventional MD (cMD) without any constraint.

The GaMD module implemented in the GPU version of AMBER18[69,70,75] was then applied to simulate the ACh-VU6007678-bound M_5 mAChR-mini-Gα_{qiN} and Iperoxo-bound M_5 mAChR-mini-Gα_{qiN} complexes. The GaMD simulations included an 8-ns short cMD run to collect the potential statistics for calculating GaMD acceleration parameters, followed by a 56-ns GaMD equilibration after adding the boost potential. Finally, three independent 500-ns GaMD production simulations were conducted for each system with randomized initial atomic velocities. The average and standard deviation (SD) of the system potential energies were calculated every 800,000 steps (1.6 ns). All GaMD simulations were performed at the "dual-boost" level, where the reference energy was set to the lower bound. One boost potential was applied to the dihedral energetic term and the other to the total potential energetic term. The upper limit of the boost potential SD (σ_0) was set to 6.0 kcal/mol for both the dihedral and the total potential energetic terms.

For each system, the three GaMD production trajectories were combined for analysis. The CPPTRAJ[76] was applied to calculate the time-courses of the root-mean-square derivations (RMSDs) of agonists and PAMs relative to the simulation starting structure, as well as the distances between VU6007678 and key interacting residues in the receptor, including $F130^{3.52}$, $R146^{4.41}$, $M150^{4.45}$, $F126^{3.48}$, $R134^{3.56}$, $V123^{3.45}$, $T133^{3.55}$ and $K141^{ICL2}$.

Acknowledgements

## Author Contributions

DMT designed the overall research. WACB, JIM, DMT designed, expressed, and purified protein samples. JIM, HV performed sample vitrification and cryo-EM imaging. WACB, JIM, DMT processed the EM data and generated and analysed atomic models. JW, KJ, YM designed, performed, and analysed MD simulations. WACB, BR, PRG, MY generated DNA constructs and performed pharmacology experiments. WACB, BR, PRG, MY, AC, CV, and DMT analysed pharmacology data. AMB and CWL provided chemical tools. YM, AC, CV, and DMT provided supervision. WACB, JIM, DMT wrote the manuscript with contributions and input from all authors.

Competing Interests.

AC is a co-founder and holds equity in Septerna Inc. The remaining authors declare no competing interests.
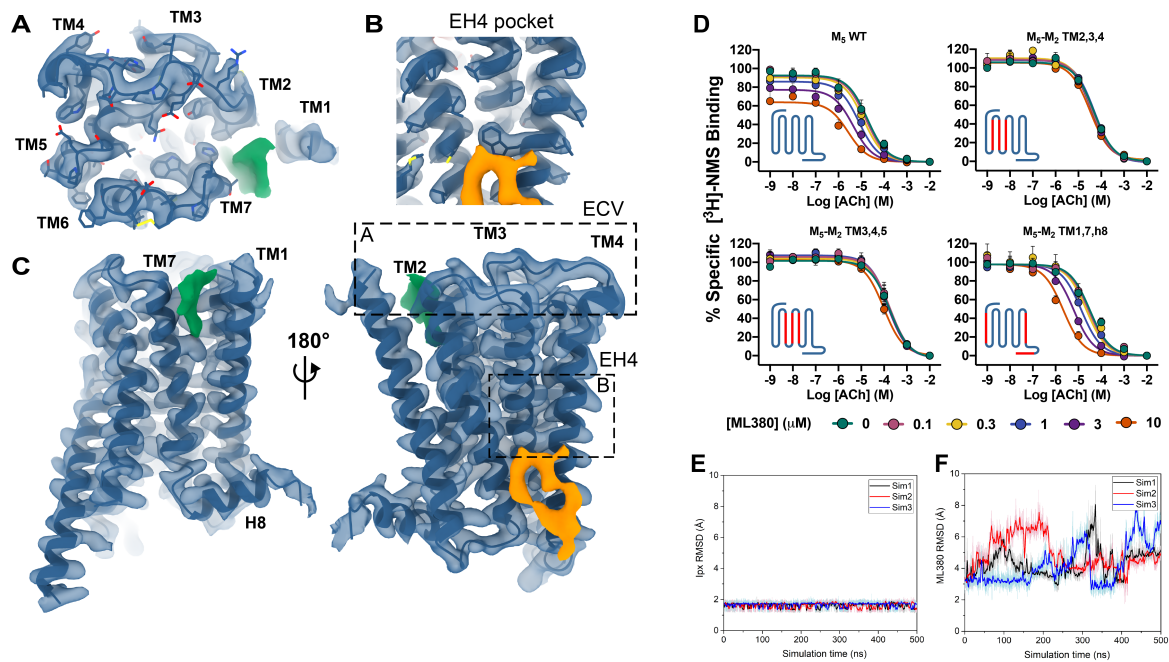
Figures
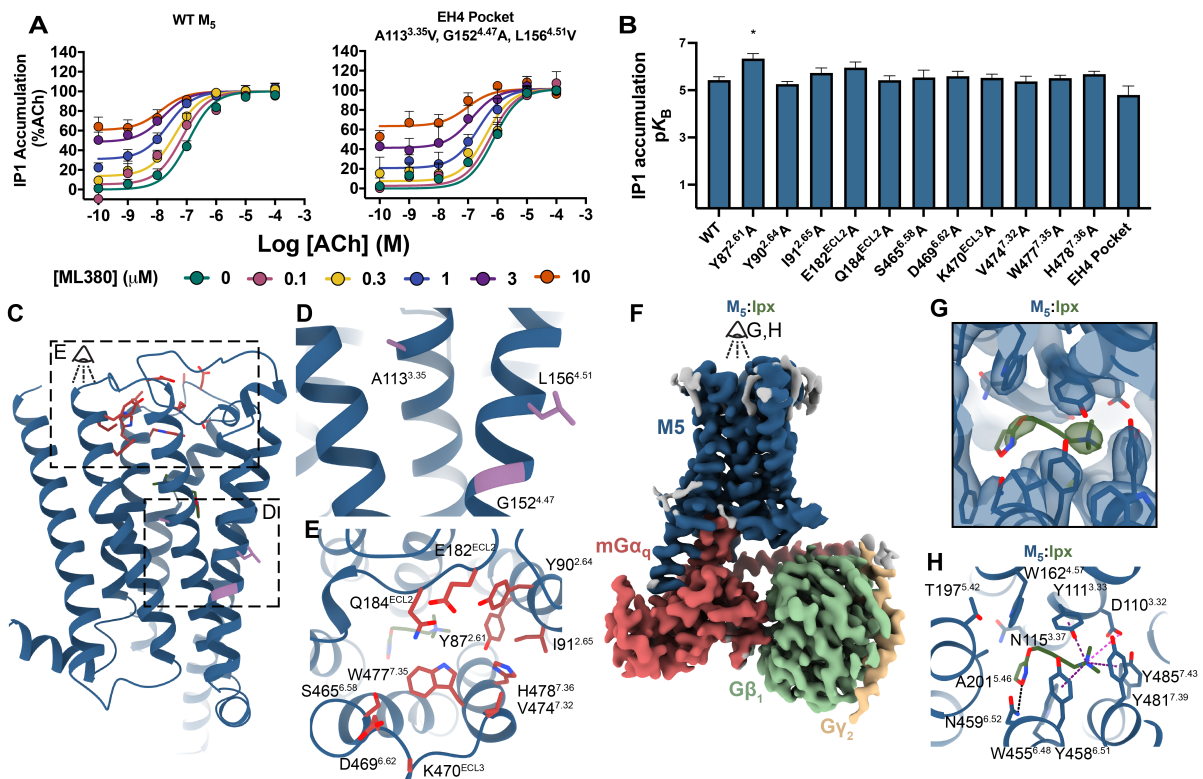
Figure 1. Structural and functional analysis of ligand-receptor interactions at the M$_5$ mAChR. **(A)** Interaction of ML380 with ACh in an IP1accumulation assay at WT M$_5$ mAChR (left) or M$_5$ EH4 pocket mutant mAChR (right) expressing CHO cells. Data points represent mean ± SEM of three to seven individual experiments performed in duplicate. WT M$_5$ mAChR n = 7, M$_5$ EH4 pocket mutant n = 3. An operational model of allosterism was fit to the data. **(B)** Effects of the M$_5$ mAChR mutations on the pK_B of ML380. Data represent the mean ± SEM of three to seven independent experiments performed in duplicate. WT M$_5$ mAChR n = 7, all other mutants n = 3. *, significantly different from WT, p < 0.05, one-way ANOVA, Dunnett's post hoc test. Parameters obtained are listed in Supplementary Table 1. **(C)** M$_5$ mAChR mutated residues are shown on the structure of the M$_5$ mAChR. **(D)** Residues of the EH4 pocket are shown as purple sticks. **(E)** Residues of the 'common' ECV are shown as red sticks. **(F)** Consensus cryo-EM map of the M$_5$ mAChR in complex with Gα$_{mGsQi}$/Gβ$_1$γ$_2$ bound to iperoxo resolved to 2.8 Å (FSC 0.143). The receptor is shown in dark blue, the heterotrimeric G$_q$ protein is shown in red, green, and yellow for the α, β, γ subunits, respectively. **(G)** Cryo-EM density (local refined receptor map, contour level 0.36) for iperoxo in the orthosteric binding site. **(H)** Interactions of iperoxo with the orthosteric binding site. Charge-charge interactions are shown as pink dotted lines, hydrogen bonds are shown as black dotted lines while purple dotted lines represent a cation-π interaction with Y111$^{3.33}$, W455$^{6.48}$, Y458$^{6.51}$, and Y481$^{7.39}$.
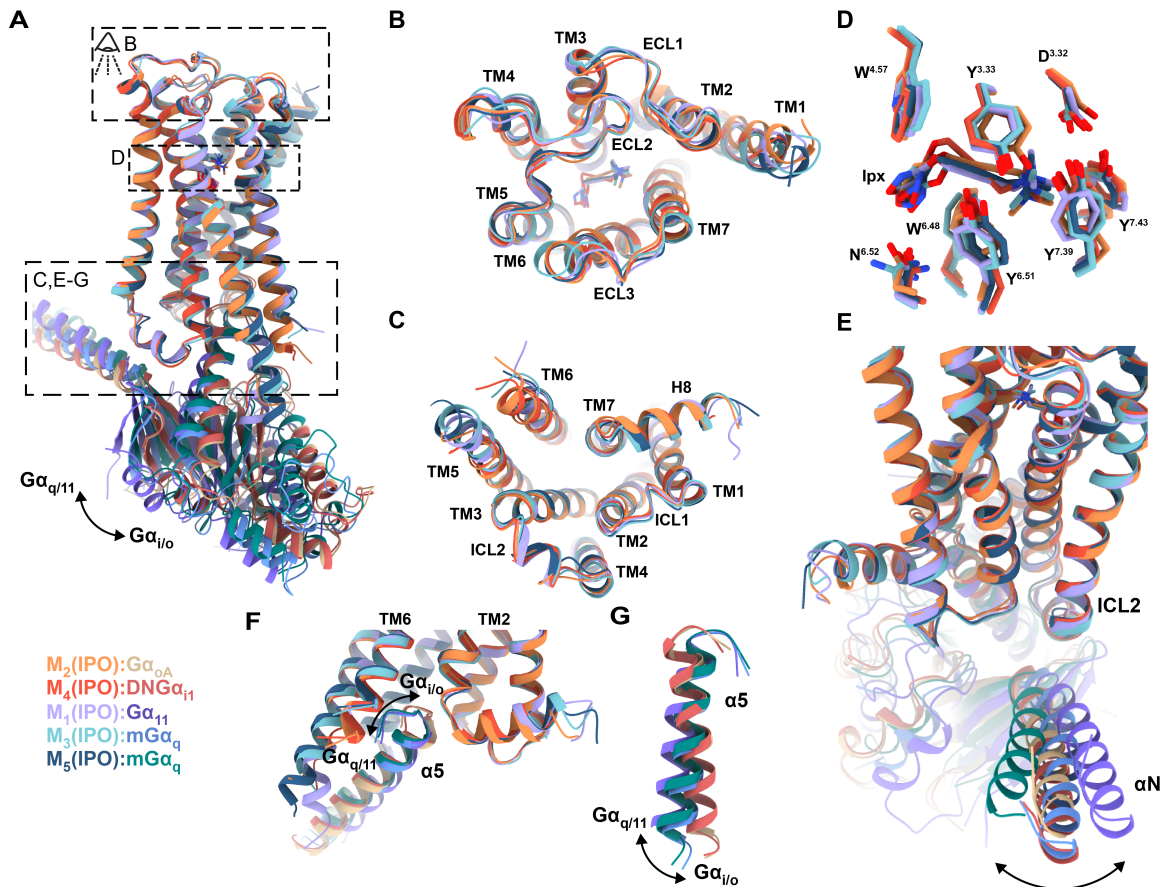
Figure 2: Structural comparison of iperoxo bound, active state M_1-M_5 mAChR structures determined by cryo-EM. (A) Overall view of the M_1 to M_5 mAChRs complexed to $G\alpha$ and bound to iperoxo. M_1-iperoxo-$G\alpha_{11}$ is coloured purple, M_2-iperoxo-$G\alpha_{oA}$ is coloured orange, M_3-iperoxo-$G\alpha_{mGsQi}$ is coloured light blue, M_4-iperoxo-dn$G\alpha_{i1}$ is coloured red, M_5-iperoxo-$G\alpha_{mGsQi}$ is coloured dark blue. **(B)** Extracellular view comparing ECLs and TM regions across the M_1 to M_5 mAChRs. **(C)** Intracellular view (G protein removed) comparing ICLs and TM regions across the M_1 to M_5 mAChRs. **(D)** Overlay of iperoxo and orthosteric binding site residues at the M_1 to M_5 mAChRs. **(E)** Intracellular view comparing the αN movement of $G\alpha$ at M_1 to M_5 mAChRs. Changes in orientation is indicated by an arrow. **(F)** Intracellular view comparing the $\alpha5$ insertion of $G\alpha$ into the M_1 to M_5 mAChRs. Changes in insertion is indicated by an arrow. **(G)** Intracellular view comparing the $\alpha5$ rotation of $G\alpha$ relative to M_1 to M_5 mAChRs. Changes in rotation is indicated by an arrow.

Figure 3: Potential cryo-EM density for ML380. (A-C) Local refined receptor cryo-EM map of the M_5 mAChR (contour level 0.3). No density for ML380 was observed in the (A) 'common' ECV (B) or in the EH4 pocket. (C) potential density for ML380 was observed parallel to TM1 and TM7 (coloured green) and at the bottom of the TM2,3,4 interface (coloured orange). **(D)** [^{3}H]-NMS equilibrium radioligand binding studies between [^{3}H]-NMS, ACh and ML380 at the WT M_5 mAChR and M_5-M_2 TM chimeric swaps. The insets are cartoons of the WT M_5 mAChR and M_5-M_2 TM chimeric swaps with blue representing M_5 mAChR domains and red representing M_2 mAChR domains. Data points represent mean ± SEM of three individual experiments performed in duplicate. Data was fit to an allosteric ternary complex model. Parameters obtained are listed in Supplementary Table 3. **(E-F)** Root mean square deviations (RMSDs) of (E) iperoxo in the orthosteric binding pocket and (F) ML380 at the potential allosteric binding site at the bottom of the TM2,3,4 interface calculated from Gaussian accelerated molecular dynamics (GaMD) simulations of the cryo-EM structure, each performed with three separate replicates indicated with different coloured traces.
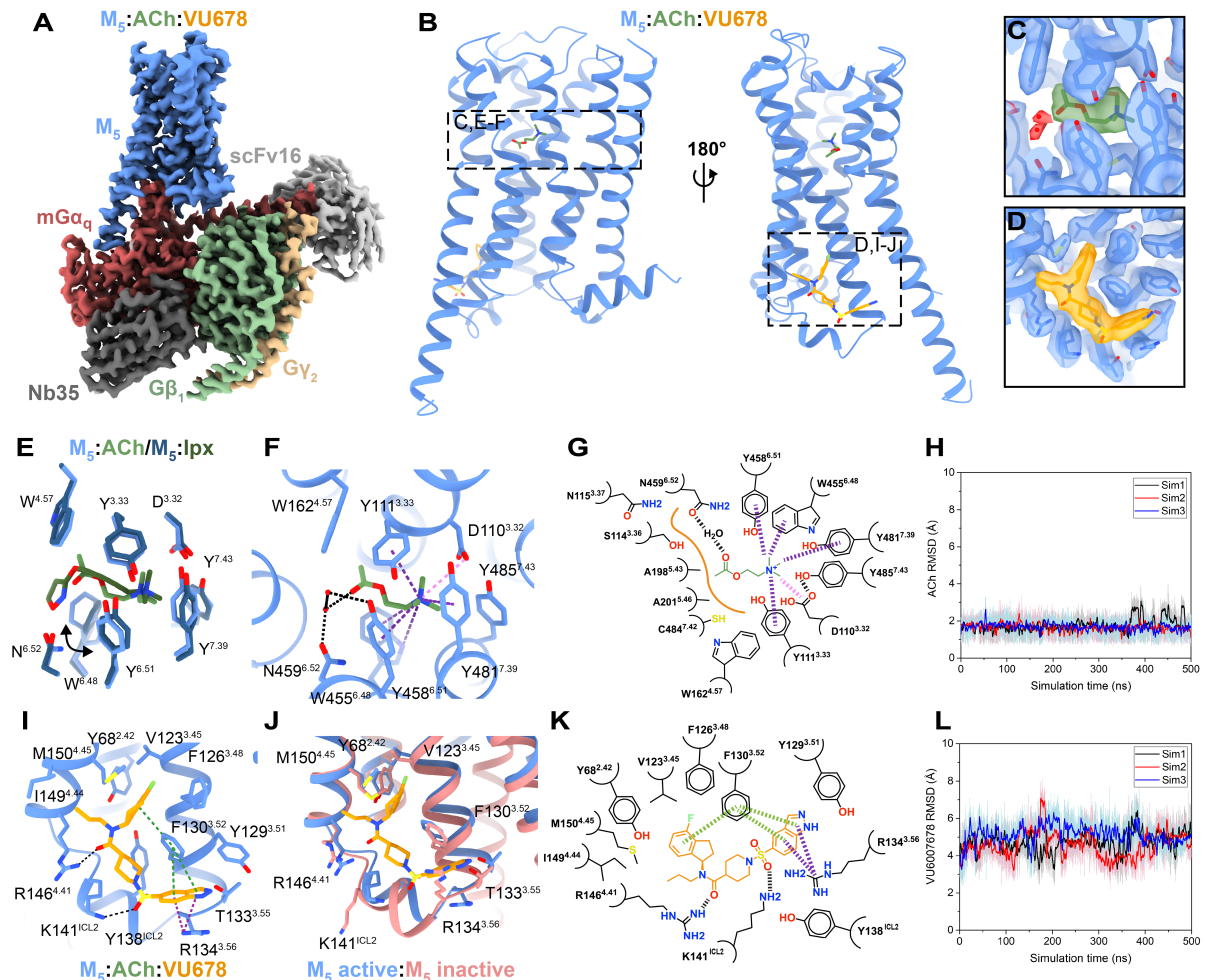
Figure 4: High resolution structure of ACh and VU6007678 bound M$_5$ mAChR in complex with heterotrimeric G protein. (A) Consensus cryo-EM map of the M$_5$ mAChR in complex with Gα$_{mGsQi}$/Gβ$_1$γ$_2$ bound to ACh and VU6007678 resolved to 2.1 Å (FSC 0.143). The receptor is shown in light blue, the heterotrimeric G$_q$ protein is shown in red, green, and yellow for the α, β, γ subunits, respectively, scFv16 is shown in light grey and Nb35 is shown in dark grey. **(B)** Model of the M$_5$ mAChR showing ACh (green) in the orthosteric binding site and VU6007678 (orange) in an allosteric binding site at the bottom at TM3 and 4 and on top of ICL2. **(C)** Cryo-EM density (local refined receptor map, contour level 0.43) for iperoxo in the orthosteric binding site. **(D)** Cryo-EM density (local refined receptor map, contour level 0.43) for VU6007678 in an allosteric binding site. **(E)** Comparison of the orthosteric binding site interactions at ACh and Ipx-bound M$_5$ mAChR. Shown in light blue sticks is ACh-bound M$_5$ mAChR residues, dark blue sticks is Ipx-bound M$_5$ mAChR residues. ACh is shown in light green sticks and Ipx is shown in dark green sticks. **(F)** Interactions of ACh with the orthosteric binding site of the M$_5$ mAChR. Charge-charge interactions are shown as pink dotted lines, hydrogen bonds are shown as black dotted lines while purple dotted lines represent a cation-π interaction with Y111$^{3.33}$, W455$^{6.48}$, Y458$^{6.51}$, and Y481$^{7.39}$. Red spheres indicate water molecules. **(G)** 2D interaction plot of ACh with the orthosteric binding site of the M$_5$ mAChR. Charge-charge interactions are shown as pink dashed lines, hydrogen bonds are shown as black dashed lines, cation-π interactions are shown as purple dashed lines and hydrophobic interactions are shown as a solid orange line. **(H)** RMSDs of ACh relative to the starting conformation in the orthosteric pocket calculated from GaMD simulations of the cryo-EM structure performed with three separate replicates indicated through different coloured traces. **(I)** Interactions of VU6007678 with its allosteric binding site at the M$_5$ mAChR. Hydrogen bonds are shown as black dotted lines, while purple dotted lines represent cation-π interactions, and green dotted lines represent π-π interactions. **(J)** Comparison of the VU6007678 allosteric

binding site to the inactive M_5 mAChR when bound to the orthosteric antagonist tiotropium (PDB:6OL9). VU6007678 is shown in orange, the M_5 mAChR bound to ACh and VU6007678 in light blue and the inactive tiotropium bound M_5 mAChR in salmon. **(K)** 2D interaction plot of VU6007678 with the its allosteric binding site. Hydrogen bonds are shown as black dashed lines, while purple dashed lines represent cation-π interactions, and green dashed lines represent π-π interactions. **(L)** RMSDs of VU6007678 relative to the starting conformation at the allosteric binding site calculated from GaMD simulations of the cryo-EM structure performed with three separate replicates indicated through different coloured traces.
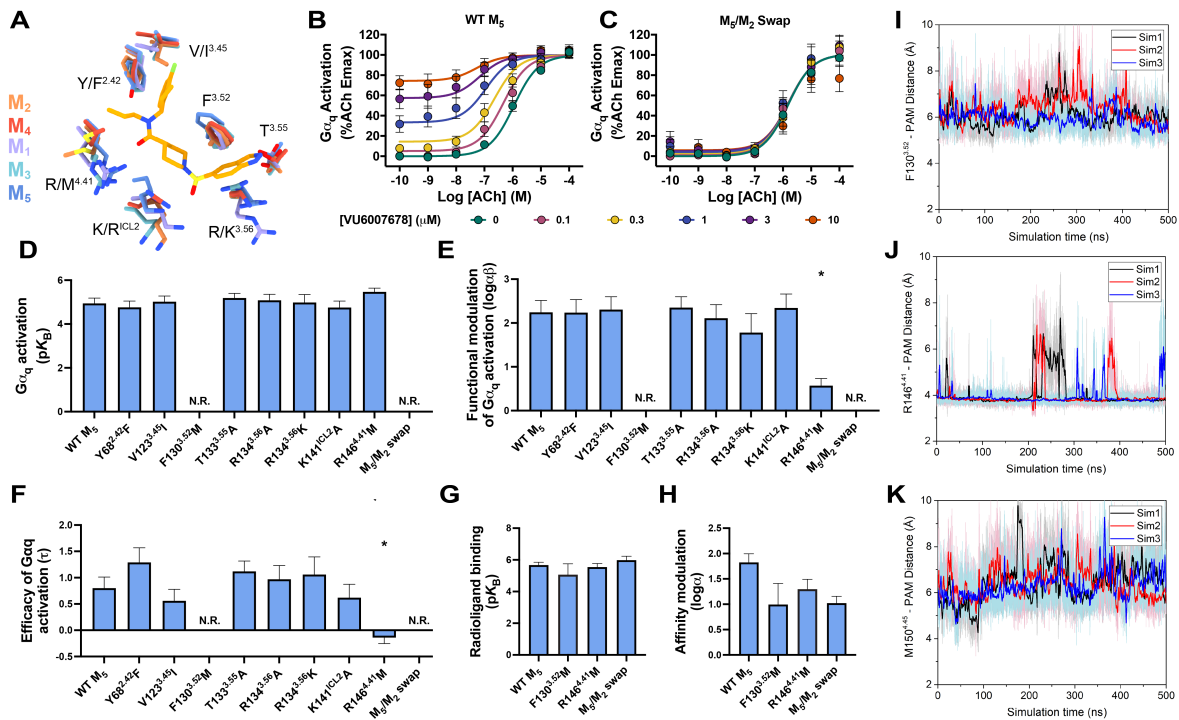
Figure 5: Structural and functional analysis of the VU6007678 allosteric binding site. **(A)** Comparison of VU6007678 allosteric binding site residues (stick representation) across the M_1-M_5 mAChRs. M_1 mAChR (PDB: 6OIJ) is shown in purple, M_2 mAChR (PDB: 6OIK) is shown in orange, M_3 mAChR (PDB: 8E9Z) is shown in light blue, M_4 mAChR (PDB: 7TRK) is shown in red and the M_5 mAChR is shown in dark blue. **(B-C)** Interaction of ML380 with ACh in Trupath G protein activation assay in (B) WT M_5 mAChR or (C) M_5/M_2 swap expressing CHO cells. Data points represent mean ± SEM of three to eight individual experiments performed in duplicate. WT M_5 mAChR n = 8, M_5/M_2 swap mutant n = 3. An operational model of allosterism was fit to the data. **(D-F)** Key pharmacological parameters for the interaction of ACh and VU6007678 in $G\alpha_q$ activation at WT M_5 mAChR and mutants. Data points represent mean ± SEM of three to eight individual experiments performed in duplicate. WT M_5 mAChR n = 8, M_5/M_2 swap, F130$^{3.52}$M, T133$^{3.55}$A, R134$^{3.56}$A, R134$^{3.56}$K mutants n = 3, Y68$^{2.42}$F, V123$^{3.45}$I, K141^{ICL2}A, R146$^{4.41}$M mutants n = 4. An operational model of allosterism was fit to the data. Parameters obtained are listed in Supplementary Table 4. **(G)** Affinity of VU6007678 (pK_B) and **(H)** logarithm of affinity cooperativity (logα) between the orthosteric agonist (ACh) and allosteric modulator (VU6007876) at the WT M_5 mAChR and selected mutants obtained in [^{3}H]-NMS equilibrium radioligand binding studies between ACh, VU6007678 and [^{3}H]-NMS. Data points represent mean ± SEM of three to five individual experiments performed in duplicate. WT M_5 mAChR n = 3, F130$^{3.52}$M, R146$^{4.41}$M n = 4, M_5/M_2 swap n = 5. Data was fit to an allosteric ternary complex model. Parameters obtained listed in Supplementary Table 4. **(I-K)** Time courses of distances from VU6007678 to (I) F130$^{3.52}$, (J) R146$^{4.41}$, (K) M150$^{4.45}$ in Å calculated from GaMD simulations performed with three separate replicates as indicated through different coloured traces.
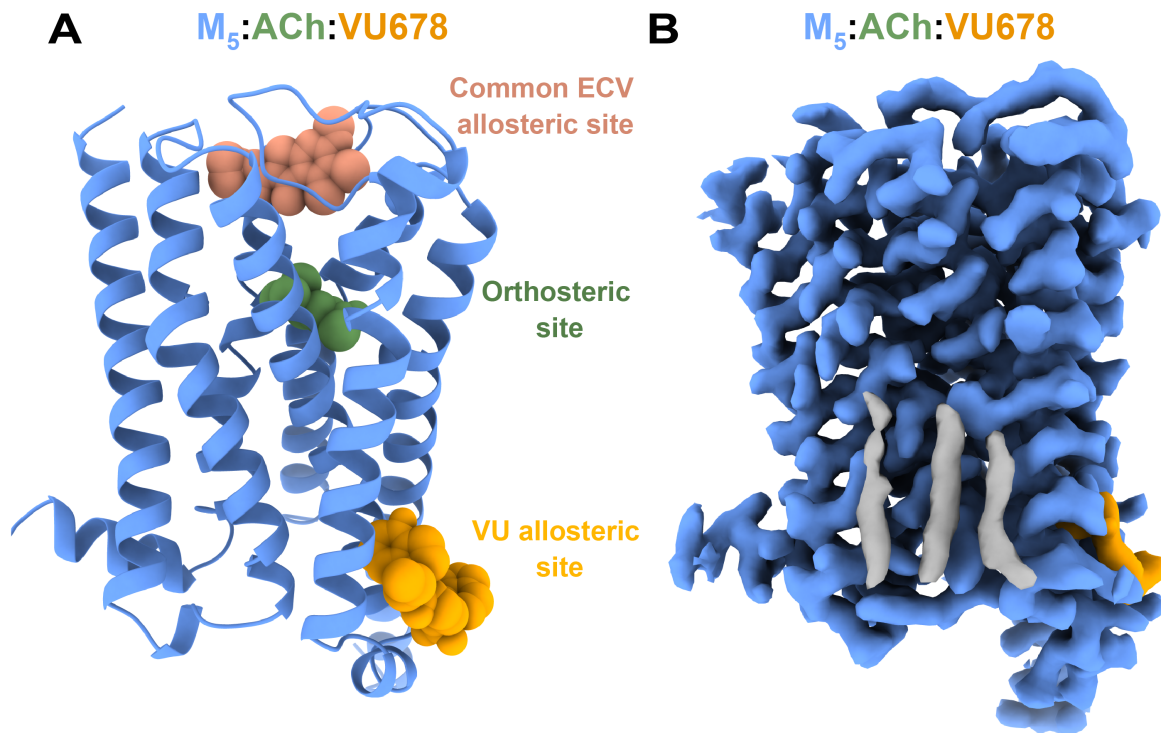
Figure 6: Allosteric sites at the mAChRs. (A) Model of the ACh-VU6007678 bound M_5 mAChR showing the novel allosteric binding site discovered for VU6007678 (orange spheres) and the 'common' ECV allosteric site occupied by LY2119620 (salmon spheres). ACh is shown as green spheres in the orthosteric binding site. **(B)** Cryo-EM density (contour level 0.47) for lipid molecules observed at the bottom of TM2,3,4 in the orthosteric binding site.

References

1. Bender, A. M., Garrison, A. T. & Lindsley, C. W. The Muscarinic Acetylcholine Receptor M5: Therapeutic Implications and Allosteric Modulation. *ACS Chemical Neuroscience* **10**, 1025–1034 (2019).

2. Vilaro, T. M., Palacios, J. M. & Mengod, G. Localization of m5 muscarinic receptor mRNA in rat brain examined by in situ hybridization histochemistry. *Neuroscience Letters* **114**, 154–159 (1990).

3. Weiner, D. M., Levey, A. I. & Brann, M. R. Expression of muscarinic acetylcholine and dopamine receptor mRNAs in rat basal ganglia. *Proceedings of the National Academy of Sciences* **87**, 7050–7054 (1990).

4. Yasuda, R. P. *et al.* Development of antisera selective for m4 and m5 muscarinic cholinergic receptors: Distribution of m4 and m5 receptors in rat brain. *Molecular Pharmacology* **43**, 149–157 (1993).

5. Foster, D. J. *et al.* M5 receptor activation produces opposing physiological outcomes in dopamine neurons depending on the receptor's location. *Journal of Neuroscience* **34**, 3253–3262 (2014).

6. Forster, G. L., Yeomans, J. S., Takeuchi, J. & Blaha, C. D. M5 Muscarinic Receptors Are Required for Prolonged Accumbal Dopamine Release after Electrical Stimulation of the Pons in Mice. *The Journal of Neuroscience* **21**, (2002).

7. Garrison, A. T. *et al.* Development of VU6019650: A Potent, Highly Selective, and Systemically Active Orthosteric Antagonist of the M5 Muscarinic Acetylcholine Receptor for the Treatment of Opioid Use Disorder. *J. Med. Chem.* **65**, 6273–6286 (2022).

8. Orsi, D. L. *et al.* Discovery of a potent M5 antagonist with improved clearance profile. Part 2: Pyrrolidine amide-based antagonists. *Bioorganic & Medicinal Chemistry Letters* **78**, 129021 (2022).

9. Fink-Jensen, A. *et al.* Role for M5 muscarinic acetylcholine receptors in cocaine addiction. *Journal of Neuroscience Research* **74**, 91–96 (2003).

10. Berizzi, A. E. *et al.* Muscarinic M5 receptors modulate ethanol seeking in rats. *Neuropsychopharmacology* **43**, 1510–1517 (2018).

11. Gunter, B. W. *et al.* Selective Inhibition of M5 Muscarinic Acetylcholine Receptors Attenuates Cocaine Self-Administration in Rats. *Addictive Biology* **23**, 1106–1116 (2018).

12. Gould, R. W. *et al.* Acute Negative Allosteric Modulation of M5 Muscarinic Acetylcholine Receptors Inhibits Oxycodone Self-Administration and Cue-Induced Reactivity with No Effect on Antinociception. *ACS Chemical Neuroscience* **10**, 3740–3750 (2019).

13. Nunes, E. J. *et al.* Examining the role of muscarinic M5 receptors in VTA cholinergic modulation of depressive-like and anxiety-related behaviors in rats. *Neuropharmacology* 108089 (2020).

14. Walker, L. C. *et al.* Muscarinic M4 and M5 receptor subtypes in the ventral subiculum differentially modulate alcohol seeking vs consumption in male alcohol preferring rats. *British Journal of Pharmacology* **178**, 3730–3746 (2021).

15. Basile, A. S. *et al.* Deletion of the M5 muscarinic acetylcholine receptor attenuates morphine reinforcement and withdrawal but not morphine analgesia. *Proceedings of the National Academy of Sciences* **99**, 11452–11457 (2002).

16. Yamada, M. *et al.* Cholinergic dilation of cerebral blood vessels is abolished in M5 muscarinic acetylcholine receptor knockout mice. *Proceedings of the National Academy of Sciences* **98**, 14096–14101 (2001).

17. Araya, R. *et al.* Loss of M5 muscarinic acetylcholine receptors leads to cerebrovascular and neuronal abnormalities and cognitive deficits in mice. *Neurobiology of Disease* **24**, 334–344 (2006).

18. Vuckovic, Z. *et al.* Crystal structure of the M5 muscarinic acetylcholine receptor. *Proceedings of the National Academy of Sciences* **116**, 26001–26007 (2019).

19. Burger, W. A. C., Sexton, P. M., Christopoulos, A. & Thal, D. M. Toward an understanding of the structural basis of allostery in muscarinic acetylcholine receptors. *Journal of General Physiology* **150**, 1360–1372 (2018).

20. Foster, D. J. & Conn, P. J. Allosteric Modulation of GPCRs: New Insights and Potential Utility for Treatment of Schizophrenia and Other CNS Disorders. *Neuron* **94**, 431–446 (2017).

21. Bridges, T. M. *et al.* Discovery of the first highly M5-preferring muscarinic acetylcholine receptor ligand, an M5 positive allosteric modulator derived from a series of 5-trifluoromethoxy N-benzyl isatins. *Journal of Medicinal Chemistry* **52**, 3445–3448 (2009).

22. Bridges, T. M. *et al.* Chemical lead optimization of a pan Gq mAChR M1, M3, M5 positive allosteric modulator (PAM) lead. Part I: Development of the first highly selective M5 PAM. *Bioorganic and Medicinal Chemistry Letters* **20**, 558–562 (2010).

23. Gentry, P. R. *et al.* Discovery of the first M5-selective and CNS penetrant negative allosteric modulator (NAM) of a muscarinic acetylcholine receptor: (S)-9b-(4-chlorophenyl)-1-(3,4-difluorobenzoyl)-2,3-dihydro-1 H -imidazo[2,1- a]isoindol-5(9b H)-one (ML375). *Journal of Medicinal Chemistry* **56**, 9351–9355 (2013).

24. Gentry, P. R. *et al.* Discovery of ML326: The first sub-micromolar, selective M5 PAM. *Bioorganic and Medicinal Chemistry Letters* **23**, 2996–3000 (2013).

25. Gentry, P. R. *et al.* Development of a highly potent, novel M5 positive allosteric modulator (PAM) demonstrating CNS exposure: 1-((1H-indazol-5-yl)sulfoneyl)-N-ethyl-N-(2-(trifluoromethyl)benzyl)piperidine-4-carboxamide (ML380). *Journal of Medicinal Chemistry* **57**, 7804–7810 (2014).

26. Bender, A. M. *et al.* Discovery and Optimization of Potent and CNS Penetrant M5-Preferring Positive Allosteric Modulators Derived from a Novel, Chiral N-(Indanyl)piperidine Amide Scaffold. *ACS Chemical Neuroscience* **9**, 1572–1581 (2018).

27. Marlo, J. E. *et al.* Discovery and Characterization of Novel Allosteric Potentiators of M1 Muscarinic Receptors Reveals Multiple Modes of Activity. *Molecular Pharmacology* **75**, 577–588 (2009).

28. Berizzi, A. *et al.* Molecular Mechanisms of Action of M5 Muscarinic Acetylcholine Receptor Allosteric Modulators. *Molecular pharmacology* **90**, 427–436 (2016).

29. Berizzi, A. E. *et al.* Structure-Activity Relationships of Pan-Gαq/11 Coupled Muscarinic Acetylcholine Receptor Positive Allosteric Modulators. *ACS Chemical Neuroscience* **9**, 1818–1828 (2018).

30. Stahl, E. & Ellis, J. Novel Allosteric Effects of Amiodarone at the Muscarinic M5 Receptor. *J Pharmacol Exp Ther* **334**, 214–222 (2010).

31. Burger, W. A. C. *et al.* Identification of a Novel Allosteric Site at the M5 Muscarinic Acetylcholine Receptor. *ACS Chemical Neuroscience* (2021).

32. Congreve, M., Oswald, C. & Marshall, F. H. Applying Structure-Based Drug Design Approaches to Allosteric Modulators of GPCRs. *Trends in Pharmacological Sciences* **38**, 837–847 (2017).

33. Kruse, A. C. *et al.* Activation and allosteric modulation of a muscarinic acetylcholine receptor. *Nature* **504**, 101–106 (2013).

34. Vuckovic, Z. *et al.* Pharmacological hallmarks of allostery at the M4 muscarinic receptor elucidated through structure and dynamics. *eLife* **12**, e83477 (2023).

35. Leach, K., Sexton, P. M. & Christopoulos, A. Allosteric GPCR modulators: taking advantage of permissive receptor pharmacology. *Trends in Pharmacological Sciences* **28**, 382–389 (2007).

36. Maeda, S., Qu, Q., Robertson, M. J., Skiniotis, G. & Kobilka, B. K. Structures of the M1 and M2 muscarinic acetylcholine receptor/G-protein complexes. *Science* **364**, 552–557 (2019).

37. Zhang, S. *et al.* Molecular basis for selective activation of DREADD-based chemogenetics. *Nature* 1–9 (2022) doi:10.1038/s41586-022-05489-0.

38. Kim, K. *et al.* Structure of a Hallucinogen-Activated Gq-Coupled 5-HT2A Serotonin Receptor. *Cell* **182**, 1574-1588.e19 (2020).

39. Mobbs, J. I. *et al.* Structures of the human cholecystokinin 1 (CCK1) receptor bound to Gs and Gq mimetic proteins provide insight into mechanisms of G protein selectivity. *PLoS Biology* **19**, 1–28 (2021).

40. Maeda, S. *et al.* Development of an antibody fragment that stabilizes GPCR/G-protein complexes. *Nature Communications* **9**, 3712 (2018).

41. Ballesteros, J. A. & Weinstein, H. Integrated methods for the construction of three-dimensional models and computational probing of structure-function relations in G protein-coupled receptors. *Methods in Neurosciences* **25**, 366–428 (1995).

42. Zhou, Q. *et al.* Common activation mechanism of class a GPCRs. *eLife* **8**, 1–31 (2019).

43. Brown, A. J. H. *et al.* From structure to clinic: Design of a muscarinic M1 receptor agonist with potential to treatment of Alzheimer's disease. *Cell* **184**, 5886–5901 (2021).

44. Hanson, M. A. *et al.* A Specific Cholesterol Binding Site Is Established by the 2.8 Å Structure of the Human β2-Adrenergic Receptor. *Structure* **16**, 897–905 (2008).

45. Thal, D. M., Glukhova, A., Sexton, P. M. & Christopoulos, A. Structural insights into G-protein-coupled receptor allostery. *Nature* **559**, 45–53 (2018).

46. Olsen, R. H. J. *et al.* TRUPATH, an open-source biosensor platform for interrogating the GPCR transducerome. *Nature Chemical Biology* **16**, 841–849 (2020).

47. Dror, R. O. *et al.* Structural basis for modulation of a G-protein-coupled receptor by allosteric drugs. *Nature* **503**, 295–299 (2013).

48. Burger, W. A. C., Draper-Joyce, C. J., Valant, C., Christopoulos, A. & Thal, D. M. Positive allosteric modulation of a GPCR ternary complex. *Science Advances* **10**, eadp7040 (2024).

49. Zhang, L., Mobbs, J. I., May, L. T., Glukhova, A. & Thal, D. M. The impact of cryo-EM on determining allosteric modulator-bound structures of G protein-coupled receptors. *Current Opinion in Structural Biology* **79**, 102560 (2023).

50. Liu, X. *et al.* Mechanism of β_2AR regulation by an intracellular positive allosteric modulator. *Science* **364**, 1283–1287 (2019).

51. Teng, X. *et al.* Ligand recognition and biased agonism of the D1 dopamine receptor. *Nat Commun* **13**, 3186 (2022).

52. Zhuang, Y. *et al.* Mechanism of dopamine binding and allosteric modulation of the human D1 dopamine receptor. *Cell Res* **31**, 593–596 (2021).

53. Xiao, P. *et al.* Ligand recognition and allosteric regulation of DRD1-Gs signaling complexes. *Cell* **184**, 943-956.e18 (2021).

54. Xu, J. *et al.* Structural and dynamic insights into supra-physiological activation and allosteric modulation of a muscarinic acetylcholine receptor. *Nat Commun* **14**, 376 (2023).

55. Taghon, G. J., Rowe, J. B., Kapolka, N. J. & Isom, D. G. Predictable cholesterol binding sites in GPCRs lack consensus motifs. *Structure* **29**, 499-506.e3 (2021).

56. Dolejší, E. *et al.* Neuroactive steroids, WIN-compounds and cholesterol share a common binding site on muscarinic acetylcholine receptors. *Biochemical Pharmacology* **192**, (2021).

57. Dolejší, E. *et al.* Neurosteroids and steroid hormones are allosteric modulators of muscarinic receptors. *Neuropharmacology* **199**, (2021).

58. Studier, F. W. Stable Expression Clones and Auto-Induction for Protein Production in E. coli. in *Structural Genomics: General Applications* (ed. Chen, Y. W.) 17–32 (Humana Press, Totowa, NJ, 2014). doi:10.1007/978-1-62703-691-7_2.

59. Zheng, S. Q. *et al.* MotionCor2: Anisotropic correction of beam-induced motion for improved cryo-electron microscopy. *Nature Methods* **14**, 331–332 (2017).

60. Zhang, K. Gctf: Real-time CTF determination and correction. *Journal of Structural Biology* **193**, 1–12 (2016).

61. Zivanov, J. *et al.* New tools for automated high-resolution cryo-EM structure determination in RELION-3. *eLife* **7**, 1–22 (2018).

62. Punjani, A., Rubinstein, J. L., Fleet, D. J. & Brubaker, M. A. cryoSPARC: Algorithms for rapid unsupervised cryo-EM structure determination. *Nature Methods* **14**, 290–296 (2017).

63. Pettersen, E. F. *et al.* UCSF ChimeraX: Structure visualization for researchers, educators, and developers. *Protein Science* **30**, 70–82 (2021).

64. Liebschner, D. *et al.* Macromolecular structure determination using X-rays, neutrons and electrons: Recent developments in Phenix. *Acta Crystallographica Section D: Structural Biology* **75**, 861–877 (2019).

65. Emsley, P., Lohkamp, B., Scott, W. G. & Cowtan, K. Features and development of Coot. *Acta Crystallographica Section D: Biological Crystallography* **66**, 486–501 (2010).

66. Williams, C. J. *et al.* MolProbity: More and better reference data for improved all-atom structure validation. *Protein Science* **27**, 293–315 (2018).

67. Berman, H., Henrick, K. & Nakamura, H. Announcing the worldwide Protein Data Bank. *Nature Structural Biology* **10**, 980–980 (2003).

68. Christopoulos, A. & Kenakin, T. G protein-coupled receptor allosterism and complexing. *Pharmacological reviews* **54**, 323–374 (2002).

69. Wang, J. *et al.* Gaussian accelerated molecular dynamics: Principles and applications. *Wiley Interdisciplinary Reviews Computational Molecular Science* **11**, e1521 (2021).

70. Miao, Y., Feher, V. A. & McCammon, J. A. Gaussian Accelerated Molecular Dynamics: Unconstrained Enhanced Sampling and Free Energy Calculation. *Journal of Chemical Theory and Computation* **11**, 3584–3595 (2015).

71. Maier, J. A. *et al.* ff14SB: Improving the Accuracy of Protein Side Chain and Backbone Parameters from ff99SB. *Journal of Chemical Theory and Computation* **11**, 3696–3713 (2015).

72. Dickson, C. J., Walker, R. C. & Gould, I. R. Lipid21: Complex Lipid Membrane Simulations with AMBER. *Journal of Chemical Theory and Computation* **18**, 1726–1736 (2022).

73. Wang, J., Wolf, R. M., Caldwell, J. W., Kollman, P. A. & Case, D. A. Development and testing of a general amber force field. *Journal of Computational Chemistry* **25**, 1157–1174 (2004).

74. Darden, T., York, D. & Pedersen, L. Particle mesh Ewald: An N·log(N) method for Ewald sums in large systems. *The Journal of Chemical Physics* **98**, 10089–10092 (1993).

75. D.A. Case, D.S. Cerutti, T.E. Cheatham, III, T.A. Darden, R.E. Duke, T.J. Giese, H. Gohlke, A.W. Goetz, D. Greene, N. Homeyer, S. Izadi, A. Kovalenko, T.S. Lee, S. LeGrand, P. Li, C. Lin, J. Liu, T. Luchko, R. Luo, D. Mermelstein, K.M. Merz, G.

Monard, H. Nguyen, I. Omelyan, A. Onufriev, F. Pan, R. Qi, D.R. Roe, A. Roitberg, C. Sagui, C.L. Simmerling, W.M. Botello-Smith, J. Swails, R.C. Walker, J. Wang, J. Wang, R.M. Wolf, X. Wu, L. Xiao, D.M. York and P.A. Kollman. *Amber 2022*. (University of California, San Francisco., 2022).

76. Roe, D. R. & Cheatham, T. E. PTRAJ and CPPTRAJ: Software for processing and analysis of molecular dynamics trajectory data. *Journal of Chemical Theory and Computation* **9**, 3084–3095 (2013).